

Microstrain distribution mapping on CuInSe₂ thin films by means of electron backscatter diffraction, X-ray diffraction, and Raman microspectroscopy

Norbert Schäfer^{a, ,}, Angus J. Wilkinson^b, Thomas Schmid^c, Aimo Winkelmann^d, Gilbert A. Chahine^e, Tobias Schüll^e, Thorsten Rissom^a, Julien Marquardt^{a, f}, Susan Schorr^{a, f}, Daniel Abou-Ras

^a Helmholtz-Zentrum Berlin für Materialien und Energie GmbH, Hahn-Meitner-Platz 1, 14109 Berlin, Germany

^b Department of Materials, University of Oxford, Parks Road, Oxford OX1 3PH, U.K

^c Federal Institute for Materials Research and Testing, Richard-Willstätter-Str. 11, 12489 Berlin, Germany

^d Bruker Nano GmbH, D-12489 Berlin, Germany

^e European Synchrotron Radiation Facility, BP 220, Grenoble Cedex, France

^f Freie Universität Berlin, Institute of Geological Sciences, Malteserstr. 74-100, 12249 Berlin, Germany

Authors' Accepted Manuscript

Version of Record was published in

Ultramicroscopy (2016)

<http://dx.doi.org/10.1016/j.ultramic.2016.07.001>

Microstrain distribution mapping on CuInSe₂ thin films by means of electron backscatter diffraction, X-ray diffraction, and Raman microspectroscopy

Norbert Schäfer^{a,*,}, Angus J. Wilkinson^b, Thomas Schmid^c, Aimo Winkelmann^d, Gilbert A. Chahine^e, Tobias Schüllie^e, Thorsten Rissom^a, Julien Marquardt^{a, f}, Susan Schorr^{a, f}, Daniel Abou-Ras

^a Helmholtz-Zentrum Berlin für Materialien und Energie GmbH, Hahn-Meitner-Platz 1, 14109 Berlin, Germany

^b Department of Materials, University of Oxford, Parks Road, Oxford OX1 3PH, U.K

^c Federal Institute for Materials Research and Testing, Richard-Willstätter-Str. 11, 12489 Berlin, Germany

^d Bruker Nano GmbH, D-12489 Berlin, Germany

^e European Synchrotron Radiation Facility, BP 220, Grenoble Cedex, France

^f Freie Universität Berlin, Institute of Geological Sciences, Malteserstr. 74-100, 12249 Berlin, Germany

Abstract

The investigation of the microstructure in functional, polycrystalline thin films is an important contribution to the enhanced understanding of structure-property relationships in corresponding devices. Linear and planar defects within individual grains may affect substantially the performance of the device. These defects are closely related to strain distributions. The present work compares electron and X-ray diffraction as well as Raman spectroscopy, which provide access to microstrain distributions within individual grains. CuInSe₂ thin films for solar cells are used as a model system. High-resolution electron backscatter diffraction and X-ray microdiffraction as well as Raman microspectroscopy were applied for this comparison. Consistently, microstrain values were determined of the order of 10⁻⁴ by these three techniques. However, only electron backscatter diffraction, X-ray microdiffraction exhibit sensitivities appropriate for mapping local strain changes at the submicrometer level within individual grains in polycrystalline materials.

1. Introduction

Thin-film solar cells with Cu(In,Ga)Se₂ absorber layers have shown power-conversion efficiencies of up to 22% [1]. The analysis of the microstructure of the Cu(In,Ga)Se₂ absorber layers is essential for the further improvement of the corresponding solar cells. Apart from the influence of grain boundaries on electrical and optoelectronic properties of Cu(In,Ga)Se₂ solar cells [2], [3] and [4], structural defects within individual grains may also affect the photovoltaic performance.

The presence of dislocation networks has been identified in Cu(In,Ga)Se₂ thin films [5] and [6]. For this polycrystalline material system, In/Ga concentrations vary strongly in the direction perpendicular to the substrate, even within individual grains [5], changing the lattice constants of the tetragonal unit cell of Cu(In,Ga)Se₂ correspondingly. Calculations in quaternary Cu(In,Ga)Se₂ performed by Balboul et al. [7] revealed that replacing about 80% of the In atoms in the CuInSe₂ lattice by Ga atoms results in strain of approx. 2×10^{-2} . Thus, for the present study, polycrystalline CuInSe₂ layers with a homogeneous distribution of the matrix elements throughout the layers were analyzed.

Strain is generally defined with respect to a specific equilibrium, as the unstrained state [8], [9], [10] and [11]. Macrostrain comprises the change of lattice parameters over a large number of grains or even over the entire polycrystalline sample, while microstrain results only from local changes within individual grains [8], [9], [10] and [11]. Considering an interplanar distance d , local strain ϵ at the position r can be defined as

$$\epsilon(r) = \frac{d(r) - d_0}{d_0} \quad \text{equation (1)}$$

with d_0 as unstrained interplanar distance. Macro- and microstrain can be formulated in a combined manner,

$$\epsilon(r) = \langle \epsilon(r) \rangle + \frac{d(r) - \langle d(r) \rangle}{d_0} \quad \text{equation (2)}$$

which leads to a constant macrostrain $\langle \epsilon(r) \rangle$ throughout the entire sample [8], [9], [10] and [11].

Therefore, care has to be taken when correlating macro- and microstrain. The deciding factor of whether techniques assess macro- or microstrain is the beam size of the radiation when impinging on the specimen surface. The polycrystalline CuInSe₂ layer studied in the present work was appropriate to access the microstrain within individual grains also by X-ray and Raman microspectroscopy with spatial resolutions in the order of few 100 nm (while few 10 nm for EBSD), since the average grain size was about 1.7 μm .

Although electron backscatter diffraction (EBSD) is established as useful technique for the mapping of crystal orientations, until recently, the determination of elastic-strain values from EBSD patterns (EBSPs) has received only little attention, because of lack in precise calibration and low qualities of the charge-couple device (CCD) cameras [12] and [13]. Determination of strain distributions using EBSD patterns is based on the cross-correlation approach, which was proposed by Troost et al. [14] as well as by Wilkinson [15] in the 1990s and is commonly known as high-resolution EBSD (HR-EBSD).

High-resolution X-ray microdiffraction (μ -HRXRD) emerged in the last years based on the improvement of the third generation synchrotron radiation facilities [16]. By using an energy-dispersive detector in combination with a white incident X-ray (micro-) beam, intra-grain variation of

d spacings of a single (hkl) spot can be acquired [17], [18] and [19]. To achieve the needed resolution in real and reciprocal space, highly focused monochromatic X-ray beam can be realized by modern beamlines, e.g. at the newly built ID01 beamline at the European Synchrotron Radiation Facility (ESRF).

Apart from X-ray and electron diffraction methods, Raman microspectroscopy is a technique to extract strain within individual CuInSe_2 grains with a mean grain-size diameter of about $1.7\mu\text{m}$ (see Appendix A). As the intensity of Raman bands depends on the relative orientations of laser polarization direction, crystal axes and direction of (optional) polarization filtering in the detection beam path, individual grains can be easily detected due to their different crystallographic orientations and distinct relative band intensities [20].

If the aim of the analysis is not just to determine an averaged microstrain value, from any measurement point or area in a grain, with respect to an unstrained reference point, but if a microstrain distribution within an individual grain is to be acquired, it is an important issue to discuss the strain sensitivity of the analysis technique applied. This is, it is necessary to elucidate the capability of this technique to distinguish unambiguously the microstrain values determined in neighboring measurement points. The strain sensitivity of HR-EBSD has been discussed based on the experimental conditions as well as on the evaluation procedures of the acquired patterns. Sensitivities ranging from $\pm 10^{-7}$ to $\pm 10^{-4}$ have been reported by various authors [12], [21], [22], [13] and [23] where the broad range of the sensitivities is due to different experimental conditions under which these values were determined; therefore, they cannot be compared with one another. For μ -HRXRD technique, Chahine et al. [17] determined strain sensitivities of below 10^{-5} . So far, no strain sensitivity value has been reported for Raman microspectroscopy, this method exhibits uncertainties concerning the detection of the peak positions of approximately 0.05 cm^{-1} when using Gaussian fits [24].

Microstrain mapping by EBSD and Raman microspectroscopy has already been reported by Vaudin et al. [25] and [26] and Friedman et al. [27], who conducted these analyses on wedge-indented Si single crystals. However, these reports do not include microstrain mapping within individual grains on the submicrometer scale [19]. The present work reports about microstrain measurements within individual grains in polycrystalline CuInSe_2 thin films by means of EBSD, X-ray microdiffraction, and Raman microspectrometry. The measured microstrain values are discussed with respect to the sensitivities and applicabilities of the techniques for microstrain mapping in polycrystalline thin-films.

2. Experimental details

2.1. Fabrication of the thin-film stacks and sample preparation

The investigated CuInSe_2 thin films were produced by three-stage co-evaporation [28] on Mo-coated glass substrates. The $\text{CuInSe}_2/\text{Mo/glass}$ stacks were completed to solar-cell devices by depositing a 50 nm thick CdS buffer layer and a window layer consisting of 125 nm i-ZnO combined with 250 nm n-ZnO on top using chemical bath deposition and radio-frequency sputtering. The thicknesses of the CuInSe_2 absorber layers were between 2 and $2.5\mu\text{m}$. The final composition

was determined by X-ray fluorescence analysis on samples produced in the same process to [Cu]=22 at.%, [In]=28 at.%, and [Se]=50 at.% with power-conversion efficiencies of between 12.2 and 13.7%. A complete description of the fabrication of the CuInSe₂ thin films can be found in the literature [28]. For EBSD and Raman microscopy, a plan-view CuInSe₂/Mo/glass sample was used. The ZnO and CdS layers of the completed solar cell were removed by etching using low-concentrated HCl, and also by bromine methanol in order to reduce the surface roughness. After etching, the surface roughness of the samples was reduced further by a final polishing step using a colloidal silica suspension (OPS by Struers). In contrast, X-ray microdiffraction was conducted on complete ZnO/CdS/CuInSe₂/Mo/glass solar cell stacks.

2.2. Basic structural and compositional characterization of investigated thin films

To ensure homogeneous elemental distributions (EDX) on microscopic and macroscopic scales, energy-dispersive X-ray spectroscopy was conducted in Zeiss Ultraplus scanning electron microscope (SEM) equipped with an Oxford Instruments XMax 80 mm² silicon drift detector on plan-view as well as on electron transparent, cross-sectional samples. In both cases, element distribution maps were acquired. EBSD orientation maps on larger scales were acquired for preliminary microstructure characterization. For EDX elemental-distribution maps, a 7 kV acceleration voltage and a 90 pA probe current were chosen. Large EBSD maps (of about View the MathML source 490µm×410µm) were acquired at 20 kV and 10 nA, using a step size of 400 nm and 4×4 detector binning.

Apart from SEM based techniques, XRD was conducted using symmetrical as well as asymmetrical geometries (see Appendix A for further details).

2.3. Conduction of strain mapping

For most strain-measurement techniques, the determination of an unstrained state of the sample or the material is necessary for defining (relative) values. Several approaches for the estimation of d_0 were discussed in literature [29]. In case of the microstrain mapping techniques, d_0 was defined either based on averages values, average obtained wavenumber, or on best image quality or highest signals. Details will be given below for each technique.

2.3.1. High-resolution electron backscatter diffraction

The HR-EBSD measurements were conducted using a Zeiss Ultraplus SEM equipped with an Oxford Instruments NordlysNano camera. Best EBSD pattern quality was achieved using an accelerating voltage of 15 kV and high beam currents up to 55 nA. Since the lattice-constant ratio c/a of the tetragonal crystal structure of CuInSe₂ is very close to 2, with a deviation of only about 0.2% [30] and [31], a pseudocubic CuInSe₂ crystal structure was assumed for the indexing of the EBSPs for simplicity.

Maps were acquired using step sizes of between 50 and 200 nm. As no hardware binning of the EBSPs was applied, the measurement durations were kept to 1 h at the longest, in order to reduce

the sample drift. The recorded EBSPs were exported from the acquisition software AZtec, and the cross-correlation was carried out by use of the commercial software CrossCourt3 (BLG Vantage). The cross-correlation analysis was conducted on patterns at a resolution of 1344×1024 pixels, using 50 regions of interest (ROI) circularly arranged around the pattern, each exhibiting a resolution of 256×256 pixels. In the present work, the reference EBSP was assigned by an algorithm referring to the image quality (IQ) of the EBSP and distances from grain boundaries. The IQ relates to the intensity of peaks obtained in the Hough transform of the EBSPs [32]. Changes in IQ can be correlated with elastic strain gradients, since severely bent or twisted planes alter the diffraction conditions within the diffracting volume. This may result in more diffuse bands within the EBSP [32] and [33]. The reference pattern was selected to correspond to the measurement point with the highest IQ of all points within a grain that were at least 100 nm away from any grain boundary. In some cases, the reference pattern was located near the position of the geometric center of the corresponding grain.

The majority of IQ values near grain boundaries were significantly smaller than those close to the centers of the grains, which can be explained by often superimposing EBSPs of the neighboring grains at grain boundaries. Tong et al. [34] have recently shown that it is still possible to successfully use cross-correlation analysis when there is some overlap but that measurement errors increase as the relative intensity of the pattern from the neighbor grain increases. In Zr, these authors estimated errors of $\approx 2 \times 10^{-4}$ when the incident beam was ≈ 18 nm from a grain boundary. To be conservative all EBSPs from regions within a grain closer than 50 nm to a grain boundary were excluded from the strain evaluation in the current work.

Following the suggestion by Britton et al. [35], rotation experiments were conducted using dynamically simulated CuInSe₂ patterns, by simulating a reference EBSP with Euler angles of [0,0,0] (according to the Bunge notation [36]) and a series of test patterns after stepwise rotations of 1 up to 10 degrees from the reference configuration, using a modified version of ESPRIT Dynamics software by Bruker Nano [37]. The cross-correlation analysis was carried out on the simulated patterns with the same parameters as for the ROIs as used for the experimental EBSPs.

2.3.2. High-resolution X-ray diffraction

μ -HRXRD measurements were performed at the ID01 beamline at the ESRF. The integral intensity of the 336 reflection was acquired at X-ray energy of 8.9 keV, a beam size of 100×100 nm² and a step size in the scan of 100 nm. Further details on the determination of the unstrained interplanar distance d_0 as well as on the evaluation and measurement routines are explained in more detail in the literature [17], [18] and [19].

2.3.3. Raman microspectroscopy

Raman maps were recorded with dimensions of up to View the MathML source 35 μ m × 35 μ m using a Horiba Jobin Yvon LabRam HR spectrometer coupled to an Olympus BX41 microscope by step-wise movement of the sample through the laser beam focused by a 100×/N.A.=0.9 objective lens using a sample-scanning stage. A step size of 200 nm was chosen, and a total of at most 30625 spectra were collected. Each spectrum was recorded within 3 – 5 s, which resulted in maximum measurement durations of about 26 h (with 3 s/spectrum) and 43 h (with 5 s/spectrum), respectively. A HeNe laser was used for excitation at $\lambda=632.8$ nm with 1 mW power reaching the sample. According to the Rayleigh criterion, the diffraction-limited lateral resolution with the objective lens and wavelength

used here is approx. 430 nm. The Raman-scattered light was dispersed by using a 1800-mm⁻¹ grating and detected by a 1024×256-pixel liquid-N₂-cooled CCD camera.

The Raman peaks for each spectrum were fitted using a Gaussian function. The complete evaluation of each spectrum, including the corresponding band shifts, was performed using a self-written National Instruments Labview routine. As the A1 mode was the most prominent and its pressure-dependence was already quantitatively described in the literature [38] and [39], band shifts around 174 cm⁻¹ were evaluated (range of the Gauss fit: 171.2–177.2 cm⁻¹). The Raman peak positions and the pressure dependence of Raman shifts for CuInSe₂ were taken from the literature [38] and [39]. Based on the pressure dependence of the A1 mode peak position described in the literature [38] and [39], wavenumber positions of the Gauss peaks were converted into stress values (in GPa). All stress values are expressed as positive or negative deviations from the average stress value of each mapped area, which was arbitrarily set to 0 GPa. Only relative changes of strain on an investigated area are given as results which allows for overcoming the problem of differences in spectrometer calibrations when comparing own with literature data. Hence the intercept of the linear relation between strain and Raman shift [38] and [39] may not be the same within the sub-wavenumber spectral resolution applied here. Only the slope of 5 cm⁻¹/GPa is used, which is much more independent from the actual spectrometer calibration. Strain values were determined from stress values by using the well-known Young's modulus of 68.8 GPa for CuInSe₂ [40] as conversion factor.

3. Results

3.1. Structural and compositional properties of the studied thin films

EBSD and EDX measurements conducted on the investigated CuInSe₂ thin film revealed a microstructure with an average grain-size diameter of about (1.75±0.02) μm, homogeneous elemental distribution, and no preferred orientation. Due to the absence of a strong preferred orientation in the investigated CuInSe₂ thin-films, we can not discuss the XRD measurements obtained in Bragg-Brentano geometry in context with the applied microstrain mapping techniques, which was, in contrast, possible for Vaudin et al. [25] and [26]. The reader is referred to Appendix A for further details.

3.2. Microstrain distributions acquired by HR-EBSD, X-ray microdiffraction and Raman microspectroscopy

As already demonstrated in a previous work [19], several techniques are able to resolve out-of-plane microstrain distribution within CuInSe₂ grains. In Fig. 1 and Fig. 2, exemplary microstrain distribution maps, acquired by HR-EBSD and μ-HR-XRD, are shown. By both techniques, relative changes in the order of 10⁻⁴ were detected. In the case of HR-EBSD, after the definition of the unstrained position within the grain, a mean value was calculated, under the simplification of normal distributed values and neglecting values near grain boundaries, to display an average-weighted map. As already mentioned, a more conservative data treatment was used considering the possible failure of the pixel-based cross-correlation approach although not every value near grain boundaries resulted in

strongly differing strain values. In some cases, values near grain boundaries in the order of 10^{-3} were obtained.

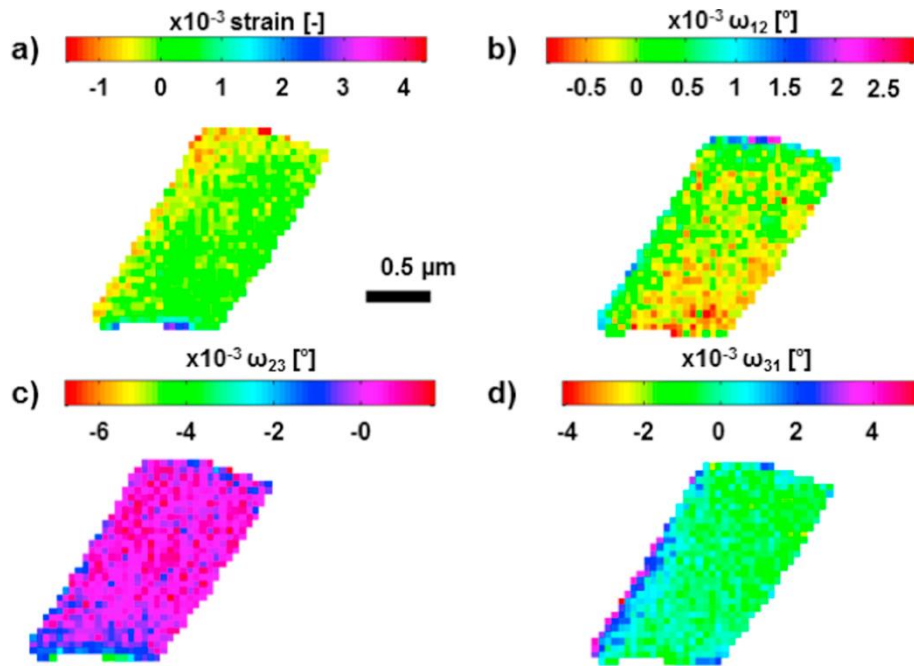


Fig. 1. a) Exemplary, average-weighted, out-of-plane microstrain distribution of one single grain acquired by cross-correlation of EBSD patterns. Highest values are likely to be measured near grain boundaries. b)-d) show the calculated rotations ω_{12} , ω_{23} and ω_{31} . Largest rotations are mostly found to be present near grain boundaries which are located at the edge of the coloring.

In Fig. 2, the integrated intensity for the probed 336 reflection measured by X-ray microdiffraction is plotted in real space tracing roughly the size and shape of the investigated grain. The position of highest intensity was assigned for the definition of d_0 , which results in the acquired microstrain distribution with relative changes of 10^{-4} . Apart from relative changes in lattice spacings, both techniques are able to extract rotations and correspondingly also tilt. The displayed rotations in Fig. 1 are based on a reference coordinate system, while the tilt distribution in Fig. 2 reflects the relative angular variation of the scattering vector in Bragg condition [17], [18] and [19]. Nevertheless, only small relative changes in angles are found, which can be considered negligible.

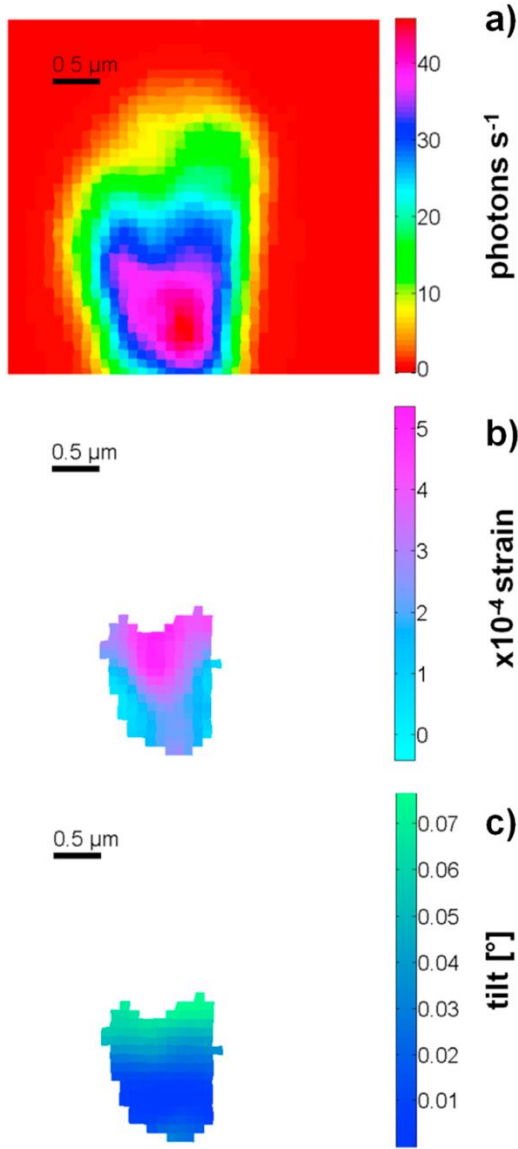


Fig. 2. a) Integrated intensity of measured 336 reflection by μ -HRXRD at an exemplary real-space position of the investigated CuInSe₂ thin-film [19]. Areas with highest intensities can be associated with one individual grain as described in the literature [19]. b) Relative microstrain distribution, where d_0 was defined by the point with the lowest tilt [19]. c) Tilt distribution of the measured 336 reflection, where the tilt is proportional to the normalized out-of-plane scattering vector [17], [18] and [19].

Fig. 3 shows a Raman intensity distribution map from an area on the CuInSe₂ layer using the A1 peak of CuInSe₂. As reported by Schmid et al. [20], individual CuInSe₂ grains can be resolved owing to the dependence of the peak intensities in Raman spectra on local crystal orientations. Based on the localization of single grains, strain distributions within selected grains can be extracted from Raman mapping data [19]. Following the intensity variation, a line scan was extracted, and the corresponding peak positions are displayed in Fig. 4. It is not possible to locate grain boundaries based only on peak positions. Within an individual grain, relative strain values were calculated to in the order of 10⁻⁴.

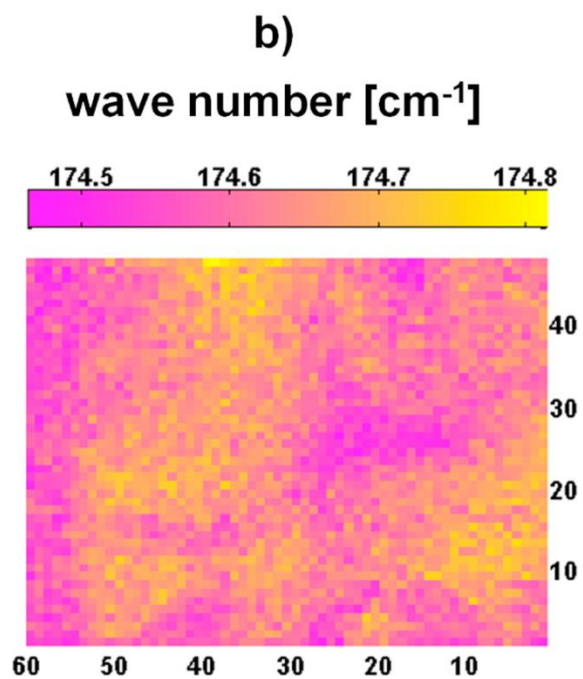
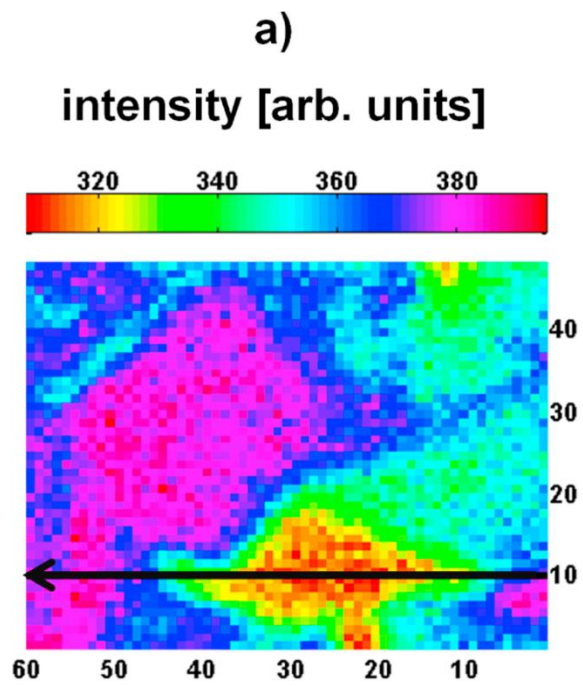


Fig. 3. a) Measured intensity distribution using the A1 peak acquired by Raman microspectroscopy. The map contains 60×48 pixels measured with a (stage) step size of 200 nm [20] and [19]. b) Corresponding distribution of the A1 peak position. These positions were fitted using a Gaussian fit as described in the literature [24] and [20].

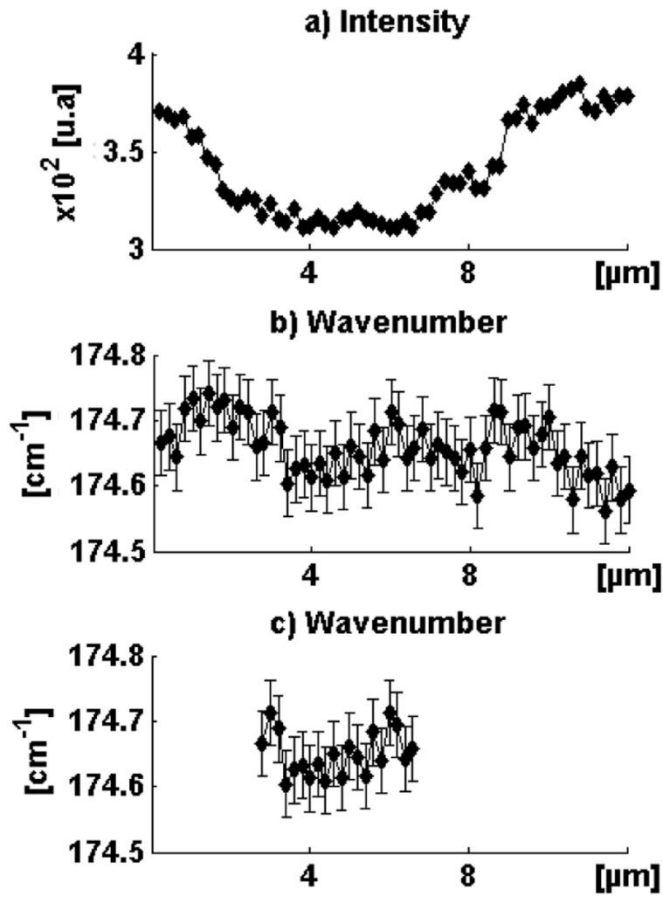


Fig. 4. a) Intensity and b) peak position line scans extracted from positions indicated in the Raman intensity map shown in Fig. 3. c) Owing to the orientation dependency of the Raman intensity of the two most prominate peaks attributed to the A1 and B2+EB2+E modes, individual grains are distinguished [19] and [20]. Errors are based on the uncertainty concerning the peak position detection of about 0.05 cm^{-1} [24].

The rotation experiments conducted on the dynamical simulated patterns resulted in the failure of the cross-correlation approach in case of rotations larger than $\theta=8^\circ$ (Fig. 5). Since only a rotation around the x_2 axis was considered within the simulation, no out-of-plane strain should be present. Based on the absolute deviation from the expected value until the threshold value of 8° , a strain sensitivity of $(2\pm 1)\times 10^{-5}$ was determined.

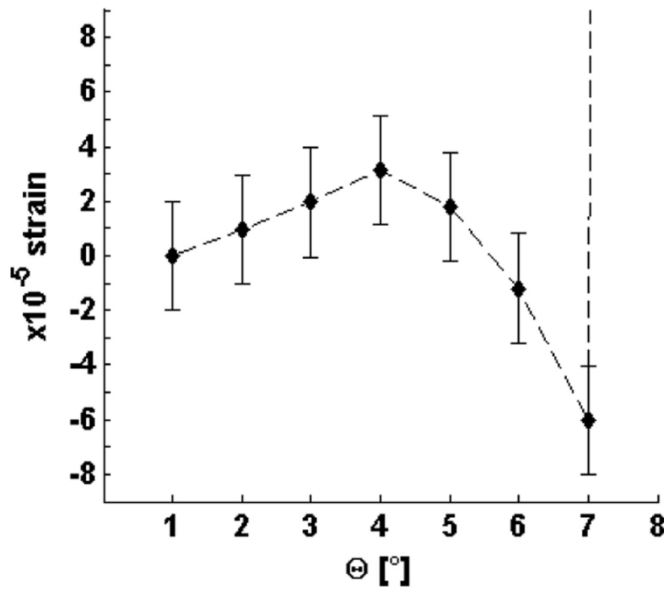


Fig. 5. Result of rotation experiment on a dynamically simulated EBSD pattern, in which out-of-plane microstrain values were determined at various rotation angles. For rotation-angle values θ of larger than 8° , the cross-correlation approach was found to fail completely. From the deviations from the measured values, a strain sensitivity of $(2\pm1)\times10^{-5}$ was calculated.

4. Discussion

Although all three techniques result in microstrain values with same orders of magnitude, the reliabilities of the acquired microstrain distributions (i.e., their sensitivities) differ substantially (see Table 1). Based on the rotation experiments on dynamical simulated patterns, a strain sensitivity of $(2\pm1)\times10^{-5}$ was estimated for EBSD, which is within the broad range of the literature values [12], [21], [22], [13] and [23] already discussed above. Nevertheless, especially considering the pixel-based cross-correlation approach, strain sensitivities always depend strongly on the experimental conditions and therefore may differ substantially, even by several orders of magnitude.

Technique		Sensitivity
HR-EBSD	exp. EBSP	$(2\pm1)\times10^{-4}$
	sim. EBSP	$(2\pm1)\times10^{-5}$
μ -HRXRD		$(3\pm1)\times10^{-5}$
Raman μ -spectroscopy		$(1\pm0.6)\times10^{-4}$

Table 1. Estimated strain sensitivities of the applied strain mapping techniques. In case of HR-EBSD, two values are given based on the conduction using simulated or experimentally acquired electron backscatter diffraction patterns.

When extracting line scans of microstrain distribution maps obtained by HR-EBSD, μ -HRXRD and Raman μ -spectroscopy (see Fig. 6), the absolute difference of two adjacent points gives the

possibility of displaying the local microstrain state independently, which is in contrast to the rotation experiment conducted on simulated patterns, where every value was compared with the initial point. In case of the extracted line scans of the HR-EBSD and μ -HRXRD microstrain distribution maps, average values of the absolute difference of two adjacent points were calculated to estimate the sensitivity. The sensitivity of Fig. 6 (c) is based on the assumptions concerning the uncertainty of 0.05 cm^{-1} in peak position determination. As shown in Fig. 6, comparison of the three techniques leads to the assumption of μ -HRXRD having the best strain resolution. HR-EBSD has also the capability of resolving strain changes within CuInSe_2 on a decent level in contrast to Raman μ -spectroscopy. The throughout mainly positive microstrain values measured by μ -HRXRD can be related to unstrained position, which was determined at the point with the smallest tilt values [19].

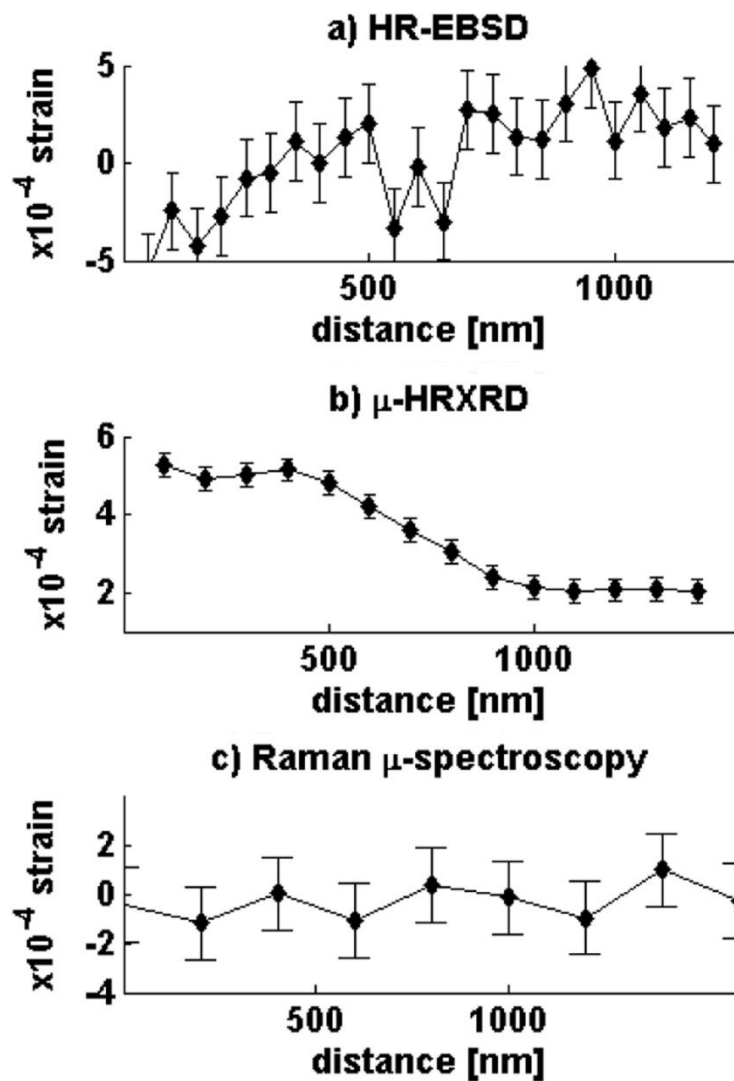


Fig. 6. Line scans at random positions of HR-EBSD, μ -HRXRD and Raman μ -spectroscopy based microstrain distributions. The error bars result from the mean average of calculated difference between measured values i and $(i+1)$ with corresponding standard deviation.

In Fig. 7, relative frequencies of the acquired microstrain distributions are plotted. The binning width for the relative frequency distribution was chosen to be 2×10^{-5} as a trade-off with respect to the calculated sensitivities (see Table 1). For all techniques, most measured microstrain changes were in the order of 10^{-4} . The estimated strain sensitivities are highlighted by grey areas, and in case of the rotation experiment conducted on dynamically simulated EBSD patterns, by a small, red area.

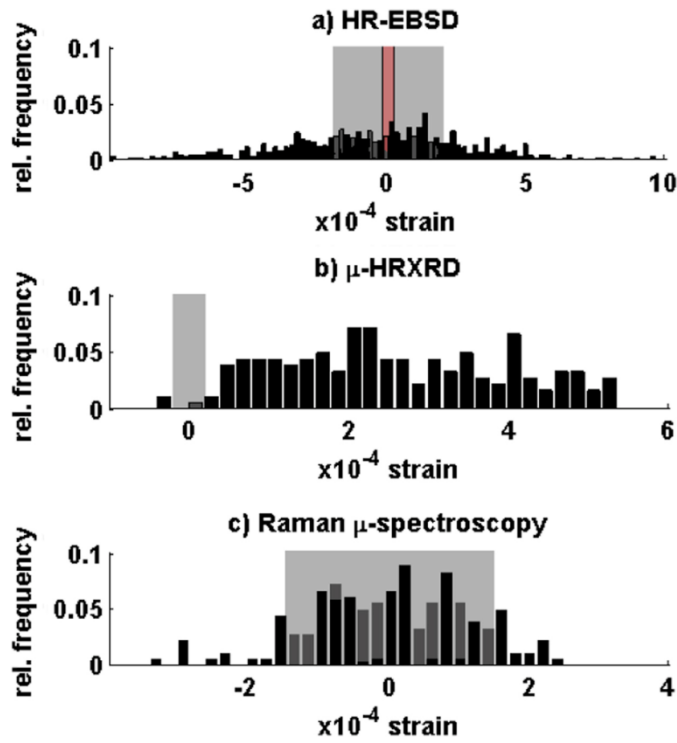


Fig. 7. Relative frequencies of microstrain values (black bars) acquired within individual grains using a) HR-EBSD, b) μ -HR-XRD and c) Raman μ -spectroscopy. For all techniques, most relative microstrain changes are in the order of 10^{-4} . Higher values resulting from the pixel-based cross-correlation are due to the influence of grain boundaries. The estimated sensitivities are given as bars by red (based on simulated EBSD) and grey (based on experimental values) colored areas. In case of Raman μ -spectroscopy, the calculated strain sensitivity exhibits the same dimension as the estimated error of the peak-position determination.

In Table 1, the calculated strain sensitivities are summarized. It can be stated that, although not exhibiting a strain sensitivity as good as μ -HR-XRD, HR-EBSD is capable of acquiring maps displaying changes of the microstrain state within an individual CuInSe_2 grain. In contrast, while the measured microstrain changes obtained by Raman microspectroscopy agree well with those measured by the other two techniques, its large strain sensitivity hampers reliable microstrain distributions for individual grains in polycrystalline material systems.

5. Conclusion

Microstrain distribution maps within individual CuInSe_2 grains were acquired by means of three different techniques, EBSD, μ -HRXRD, and Raman microspectroscopy. For most measurement points, these maps exhibit average microstrain values in the order of 10^{-4} . The three analysis methods exhibit various advantages and disadvantages. While μ -HRXRD is able to access microstrain distributions even within thin films buried in a solar-cell stack, EBSD provides the highest spatial resolution of few tens of nanometers. On the other hand, Raman microspectroscopy does not require high vacuum conditions and can be set up by a relatively small effort. Nevertheless, the large strain-sensitivity value found for Raman microspectroscopy impedes the acquisition of microstrain distributions within individual grains, while the strain sensitivities determined for μ -HRXRD and HR-EBSD provide reliably access to local microstrain changes at the submicrometer scale in various polycrystalline materials systems.

Acknowledgements

The authors would like to thank Bianca Bunn, Carola Ferber, Michael Kirsch, Tim Münchenberg, and Jan Schniebs for solar-cell processing. Ulrike Bloeck, Peter Schubert-Bischoff and Christiane Förster for their help with the sample preparation. Special thanks are due to Jenny Goulden, Frank Bauer (both Oxford Instruments), Graham Meaden (BLG Vantage), and Alfred Kuchar (Carl Zeiss Microscopy). The authors would like to thank Christoph Genzel for fruitful discussions. Financial support by the Helmholtz Virtual Institute Microstructure Control in Thin-Film Solar Cells, VI-520, is gratefully acknowledged.

Appendix A

Fig. 8, Fig. 9, Fig. 10 and Fig. 11 show the result of the initial sample characterization using large area EBSD maps. As indicated in Fig. 11, a high density of twin boundaries are found to be present within the investigated thin films.

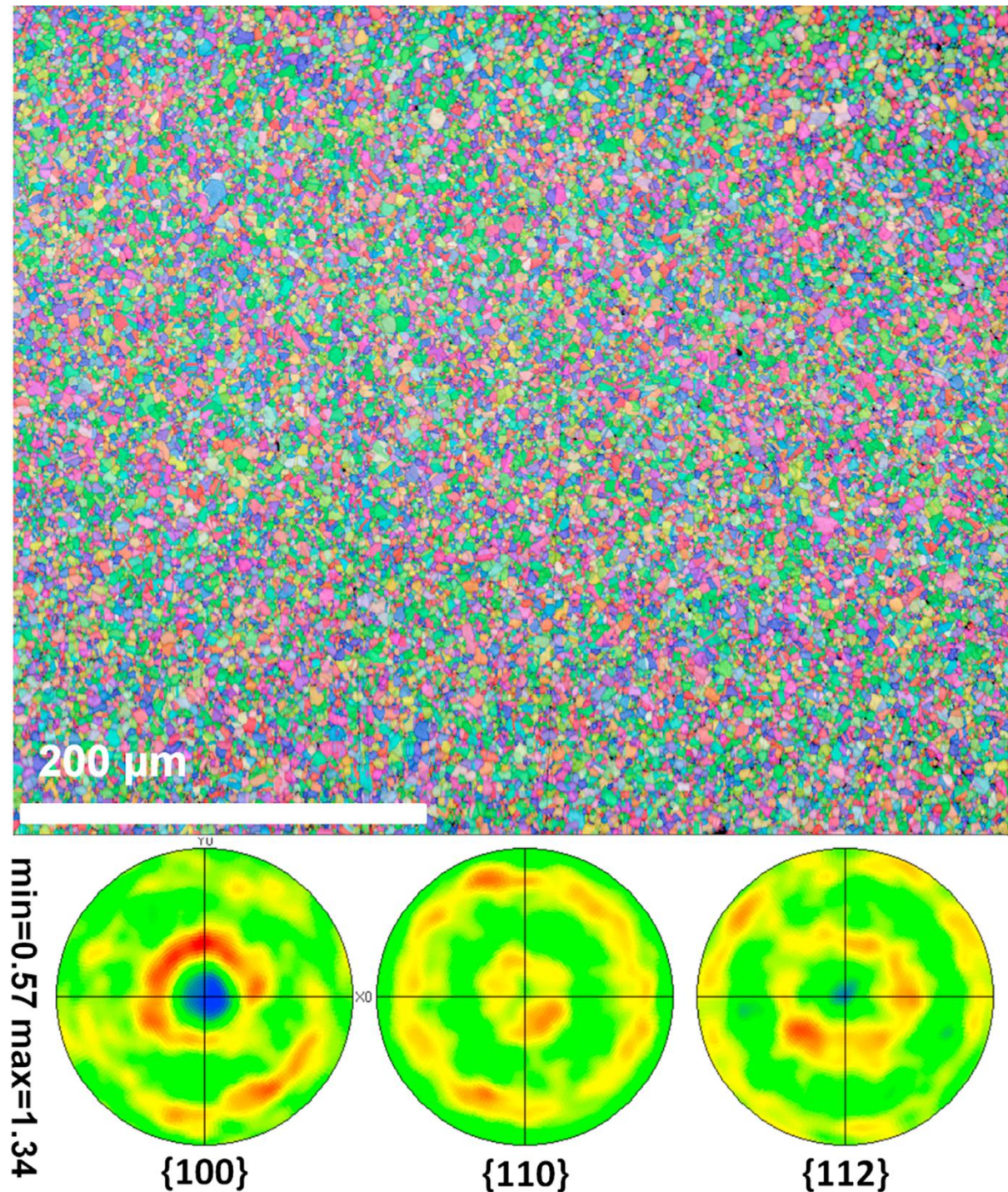


Fig. 8. EBSD orientation map including pole figures of investigated CuInSe₂/Mo/glass stack. No pronounced preferred orientation was found to be present. EBSD map was acquired at 20 kV, 10 nA probe current, using with a step size of 400 nm and 4×4 hardware binning. Approx. 1.3 million data points are used for pole figure calculation.

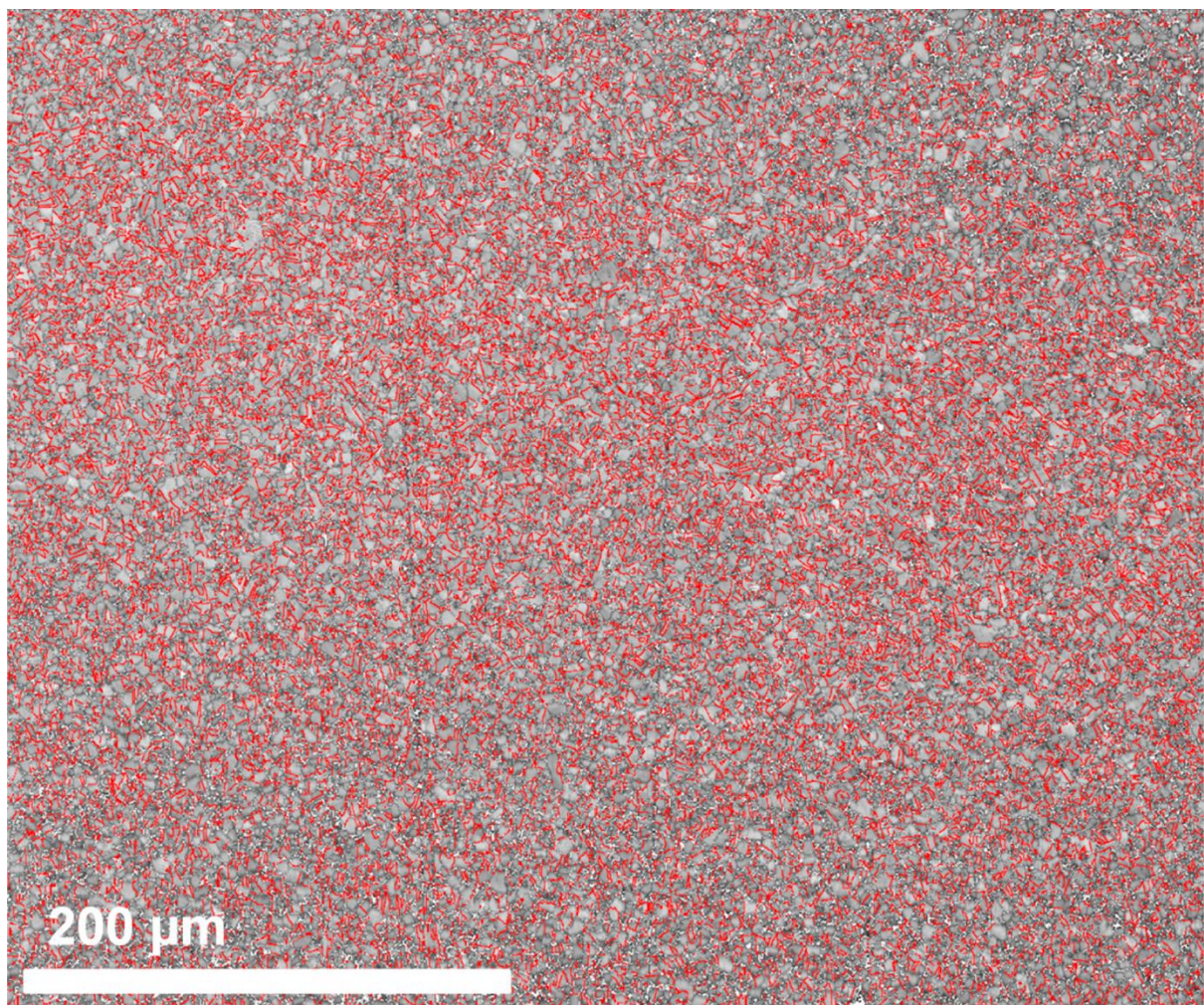


Fig. 9. Pattern-quality map (same EBSD data as for Fig. 8) with $\Sigma 3$ twin boundaries highlighted by red lines.

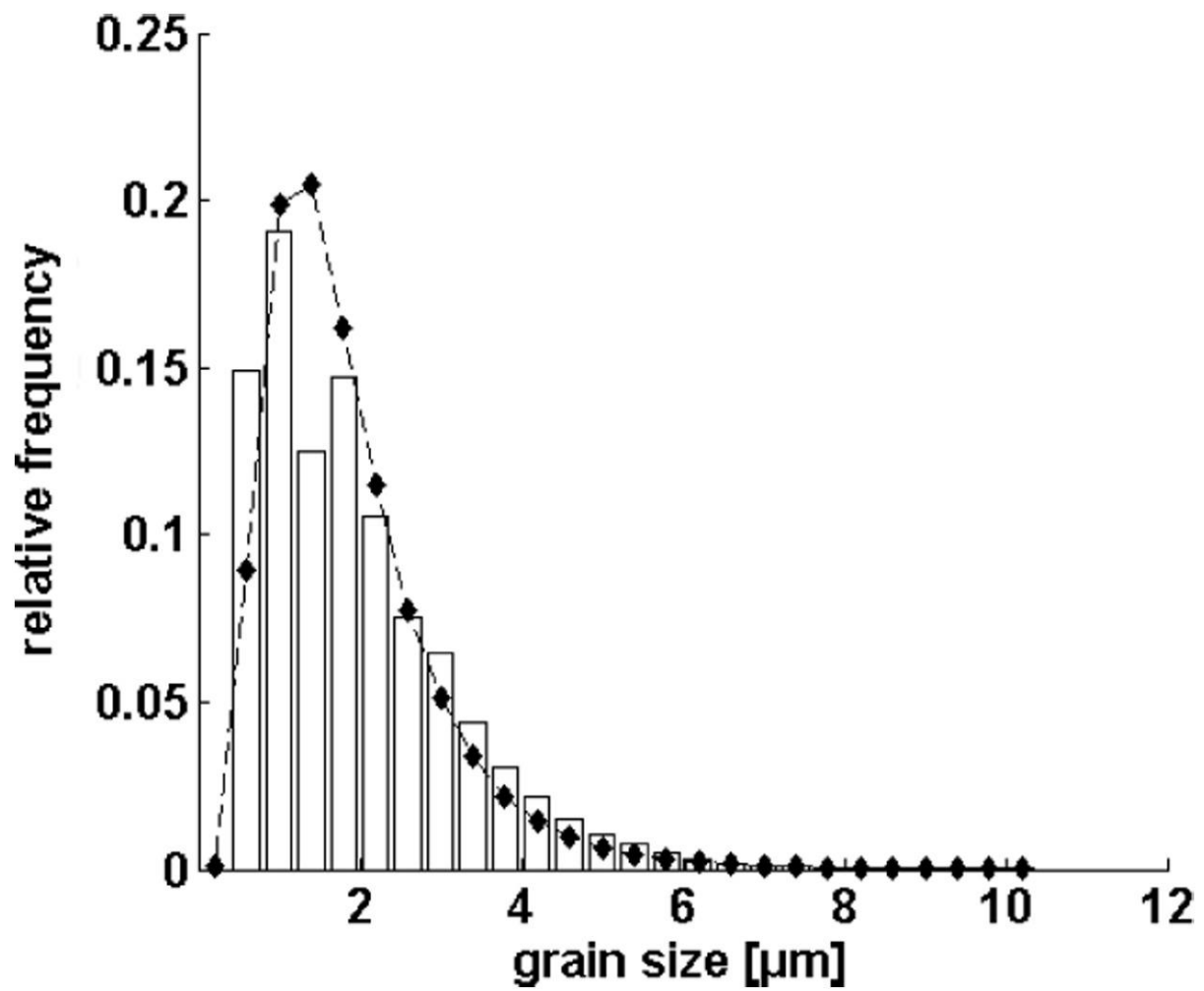


Fig. 10. Grain-size distribution of investigated CuInSe₂ thin film with an average value of around $(1.75 \pm 0.02) \mu\text{m}$. For the determination of the average grain size, a lognormal distribution function was used according to Aitchison & Brown [48] and Abou-Ras et al. [45]. In total, more than 55000 grains were considered.

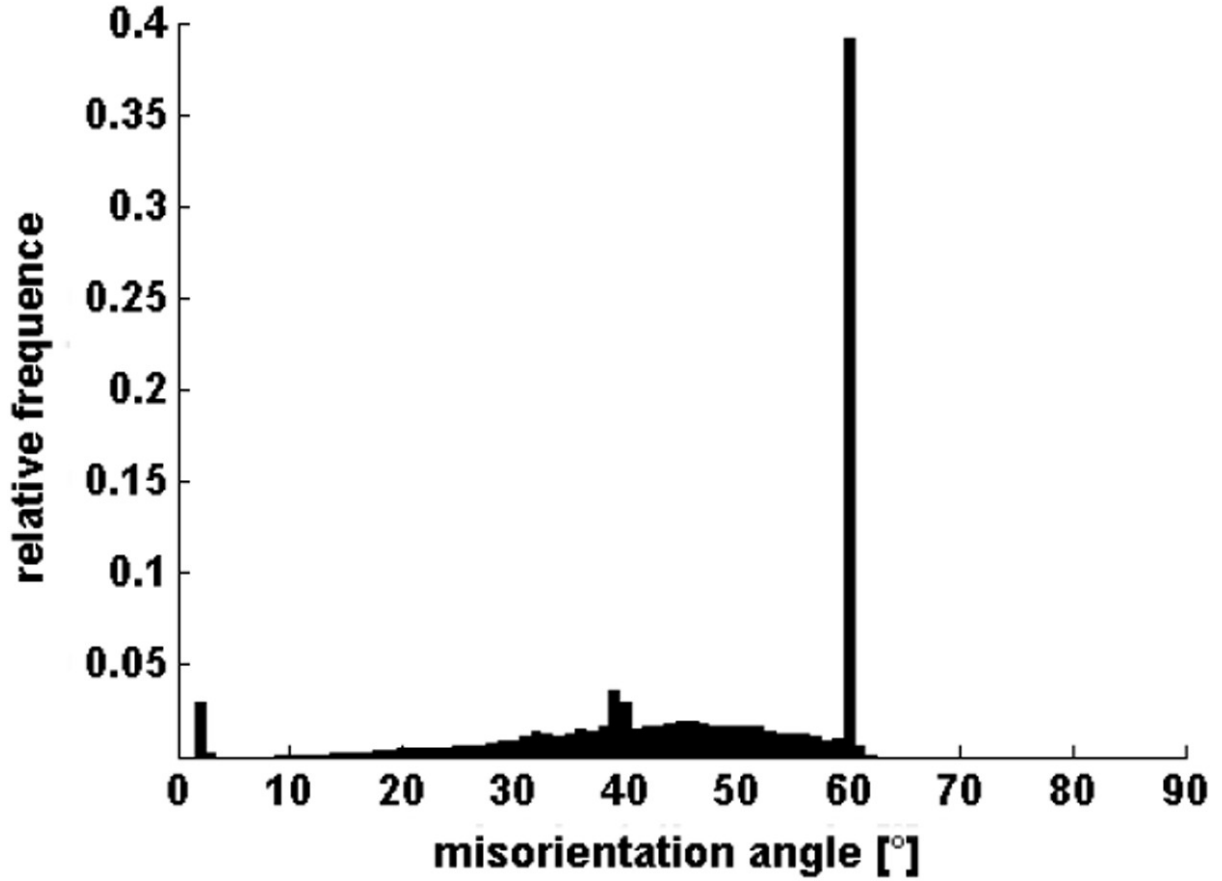


Fig. 11. Misorientation-angle distribution of investigated CuInSe₂ thin film. Local maxima are visible at around 39°/39° and 60°/60°, which can be correlated with the presence of $\Sigma 3$ and $\Sigma 9$ twin boundaries [45], [46], [47] and [49].

For initial sample characterization, before needed sample preparation, XRD patterns were acquired for three different incidence angles of 0.5, 2, and 5° using a PANalytical X'pert Pro diffractometer with a Cu-K_{1,2} source. As the diffraction volume is depending on the domain size, which should be smaller than the actual grain size, the peak broadening can directly correlated with local strain, i.e. microstrain, changes. With an attenuation coefficient $\mu(\text{CuInSe}_2)$ of about $6.34 \times 10^{-4} \text{ m}^{-1}$, 66% of the radiation was absorbed at a depth of about 1.4 m. For the incident beam a parallel beam optic, a Ni 0.02 mm filter, a 0.04 rad vertical collimator, a 1/16° divergence slit and a 2 mm mask were used for the measurements. For each scan a step size of 0.04° with time per step of 40 s was chosen. The thin film was carefully adjusted concerning the sample height to avoid the sample height error. The diffraction patterns were analyzed applying the LeBail method [41], taking into account the instrumental resolution function, which was determined for each incident angle using a LaB₆ standard (NIST-SRM 660b). The data treatment was performed using the software Fullprof [42]. In the analysis a Pseudo-Voigt function, which relates the integral peak broadening to the linear combination of a Gaussian and a Lorentzian component [43] and [44], was used to describe the peak shape.

For the three chosen incidence angles of 0.5, 2, and 5° microstrain values of $(1.7 \pm 0.2) \times 10^{-3}$ for 0.5°, $(4 \pm 1) \times 10^{-4}$ for 2° and $(6.1 \pm 0.6) \times 10^{-4}$ for 5° were calculated.

Although these values were not able to be compared with the acquired distributions by means of HR-EBSD, μ -HRXRD and Raman μ -spectroscopy, the high density of twin boundaries were concurrent. As twinning is commonly reasoned for reduction of strain [45], [46] and [47], the relatively small microstrain values can be interpreted in this context. As the formation of twin boundaries in chalcopyrite is depending on the local crystallographic orientation, a relationship with microstrain is clearly present.

Appendix B

Fig. 12 and Fig. 13) show homogeneous elemental distributions of the investigated CuInSe_2 thin film. To ensure the homogeneity, plan-view as well as cross-sectional samples were investigated.

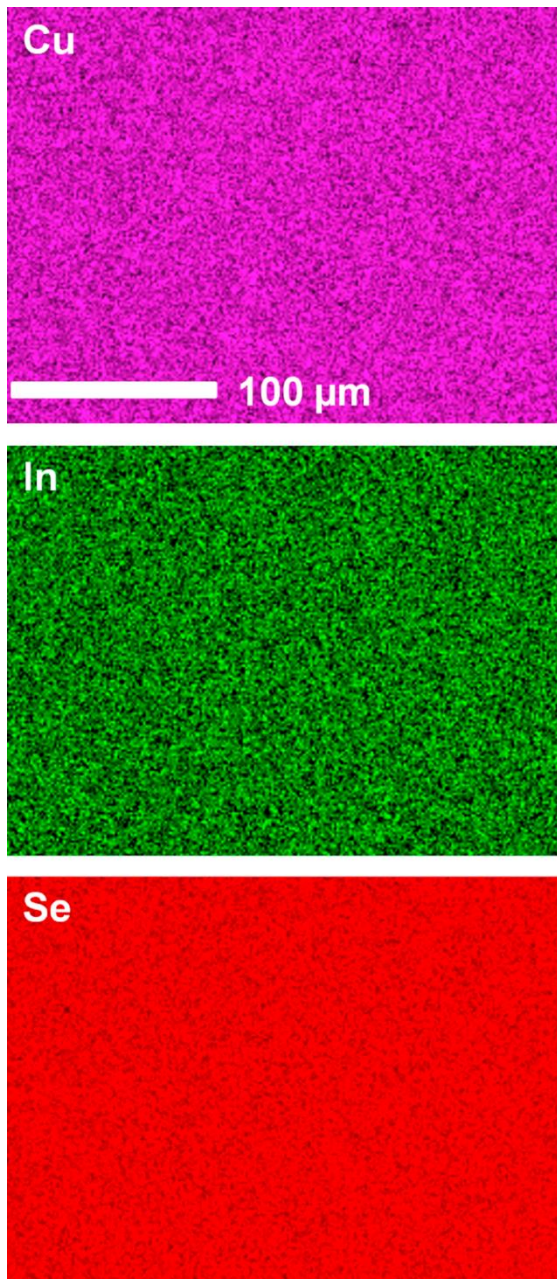


Fig. 12. EDX maps acquired on a $\text{CuInSe}_2/\text{Mo}/\text{glass}$ stack at 7 kV and around 90 pA beam current. The matrix elements Cu, In, and Se were found to be homogeneously distributed over several View the MathML source $100\mu\text{m}$.

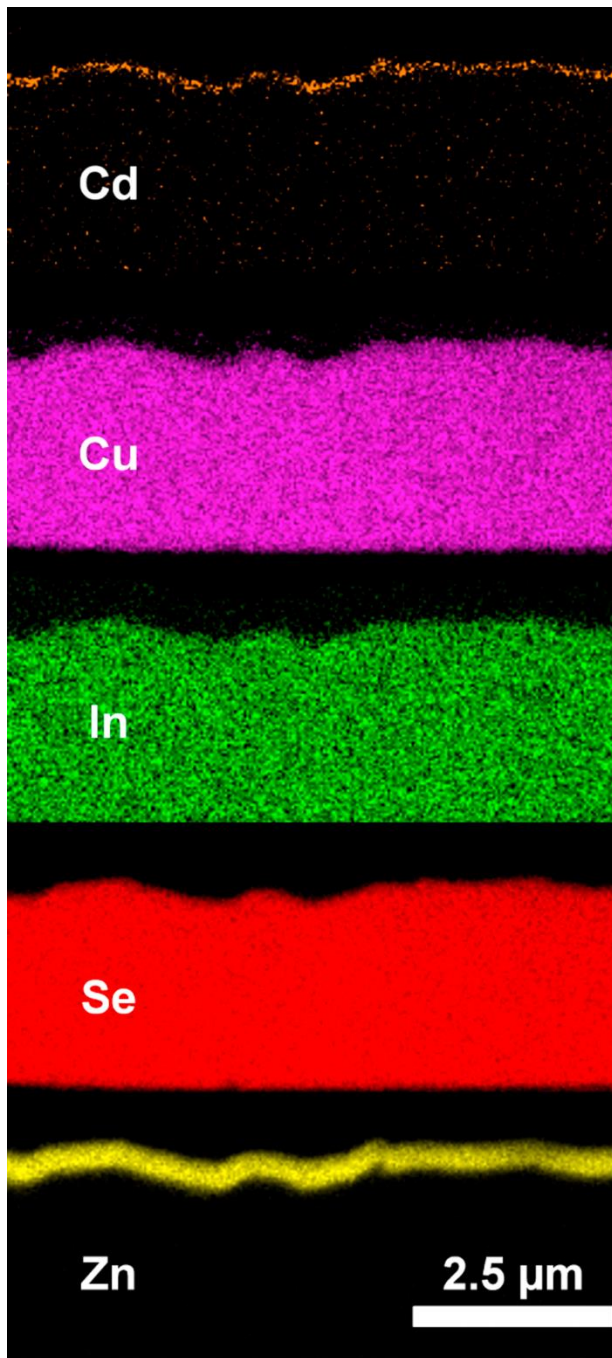


Fig. 13. Elemental distribution maps of a ZnO/CdS/CuInSe₂/Mo/glass stack. Elemental distributions were acquired at 7 kV and 90 pA beam current. Owing to the use of electron transparent sample, a spatial resolution of at least 50 nm can be achieved in even the SEM. Homogeneous elemental distributions were obtained for the matrix elements Cu, In, and Se in the CuInSe₂ thin film.

References

- [1] https://www.zsw-bw.de/fileadmin/user_upload/PDFs/Aktuelles/2016/PDFs_Presseinformationen_English/pi07-2016-ZSW-CIGS22Percent-en.pdf .
- [2] M. Nichterwitz, D. Abou-Ras, K. Sakurai, J. Bundesmann, T. Unold, R. Scheer, H.-W. Schock
Influence of grain boundaries on current collection in Cu(In,Ga)Se₂ thin-film solar cells
Thin Solid Films, 517 (2009), pp. 2554–2557 URL [⟨](#)
- [3] J. Kavalakkatt, D. Abou-Ras, J. Haarstrich, C. Ronning, M. Nichterwitz, R. Caballero, T. Rissom, T. Unold, R. Scheer, H.W. Schock
Electron-beam-induced current at absorber back surfaces of Cu(In,Ga)Se₂ thin-film solar cells
J. Appl. Phys., 115 (2014) <http://dx.doi.org/10.1063/1.4858393> 014504-1-10
- [4] M. Müller, D. Abou-Ras, T. Rissom, F. Bertram, J. Christen
Symmetry dependent optoelectronic properties of grain boundaries in polycrystalline Cu(In,Ga)Se₂ thin films
J. Appl. Phys., 115 (2014) <http://dx.doi.org/10.1063/1.4861149> 023514-1-6
- [5] J. Dietrich, D. Abou-Ras, T. Rissom, T. Unold, H.-W. Schock
Compositional Gradients in Cu(In,Ga)Se₂ Thin Films for Solar Cells and Their Effects on Structural Defects
IEEE Journal of Photovoltaics, 2 (3) (2012), pp. 364–370
- [6] C. Kiely, R. Pond, G. Kenshole, A. Rockett,
A TEM study of the crystallography and defect structures of single crystal and polycrystalline copper indium diselenide
Phil. Mag. A, 63 (1991), pp. 1249–1273 URL [⟨](#)
- [7] M.R. Balboul, H.W. Schock, S.A. Fayak, A. Abdel El-Aal, J.H. Werner, A.A. Ramadan
Correlation of structure parameters of absorber layer with efficiency of Cu(In,Ga)Se₂ solar
Appl. Phys. A, 92 (2008), pp. 557–563
- [8] E. Macherauch, H. Wohlfahrt, U. Wolfstieg
Härtereitechnische Mitteilungen (HTM), 28 (1973), pp. 201–211
- [9] H. Behnken
V. Hauk (Ed.), Some basic relations to the stress analysis using diffraction methods, Elsevier (1997)
- [10] C. Krill, R. Haberkorn, R. Birringer, Handbook of Nanostructured Materials and nanotechnology, Volume 2: Spectroscopy and Theory, Academic Press, Ch. 3, in: H.S. Nalwa (Ed.), Specification of microstructure and characterization by scattering techniques, 2000, pp. 155–211.
- [11] E.J. Mittemeijer
Fundamentals of Materials Science
Springer, Heidelberg Dordrecht London New York (2010)

- [12] A.J. Wilkinson, G. Meaden, D.J. Dingley
High resolution mapping of strains and rotations using electron backscatter diffraction
Mater. Sci. Technol., 22 (2006), pp. 1271–1278
- [13] T. Britton, J. Jiang, R. Clough, E. Tarleton, A. Kirkland, A. Wilkinson
Assessing the precision of strain measurements using electron backscatter diffraction - part 1: detector assessment
Ultramicroscopy, 135 (2013), pp. 126–135
- [14] K.Z. Troost, P. van der Sluis, D.J. Gravesteijn
Microscale elastic-strain determination by backscatter Kikuchi diffraction in the scanning electron microscope
Applied Physics Letters, 62 (10) (1993), pp. 1110–1112
- [15] A.J. Wilkinson
Measurement of elastic strains and small lattice rotations using electron back scatter diffraction
Ultramicroscopy, 62 (4) (1996), pp. 237–247
- [16] G. Ice, R. Barabash
White beam microdiffraction and dislocations gradients
F. Nabarro, J. Hirth (Eds.), *Dislocations in Solids*, 13, Elsevier (2007), pp. 499–601
- [17] G.A. Chahine, M.-I. Richard, R.A. Homs-Regajo, T.N. Tran-Caliste, D. Carbone, V.L.R. Jacques, R. Grifone, P. Boesecke, J. Katzer, I. Costina, H. Djazouli, T. Schroeder, T.U. Schüllli
Imaging of strain and lattice orientation by quick scanning X-ray microscopy combined with three-dimensional reciprocal space mapping
Journal of Applied Crystallography, 47 (2) (2014), pp. 762–769
- [18] G.A. Chahine, M.H. Zoellner, M.I. Richard, S. Guha, C. Reich, P. Zaumseil, G. Capellini, T. Schroeder, T.U. Schüllli
Strain and lattice orientation distribution in SiN/Ge complementary metal-oxide-semiconductor compatible light emitting microstructures by quick x-ray nano-diffraction microscopy
Appl. Phys. L, 106 (2015), p. 071902
- [19] N. Schäfer, G.A. Chahine, A.J. Wilkinson, T. Schmid, T. Rissom, T.U. Schüllli, D. Abou-Ras
Microstrain distributions in polycrystalline thin films measured by X-ray microdiffraction
Journal of Applied Crystallography, 49 (2) (2016), pp. 632–635
- [20] T. Schmid, N. Schäfer, S. Levchenko, T. Rissom, D. Abou-Ras
Orientation-distribution mapping of polycrystalline materials by raman microspectroscopy
Scientific Reports, 5 (2015), p. 18410
- [21] T. Britton, A. Wilkinson
Measurement of residual elastic strain and lattice rotations with high resolution electron backscatter diffraction
Ultramicroscopy, 111 (8) (2011), pp. 1395–1404

- [22] T. Britton, A. Wilkinson
High resolution electron backscatter diffraction measurements of elastic strain variations in the presence of larger lattice rotations
Ultramicroscopy, 114 (2012), pp. 82–95
- [23] A.J. Wilkinson, D.J. Dingley, G. Meaden
Strain mapping using electron backscatter diffraction
A.J. Schwartz, M. Kumar, B.L. Adams, D.P. Field (Eds.), *Electron Backscatter Diffraction in Materials Science*, Springer, US (2009), pp. 231–249
- [24] M. Becker, H. Scheel, S. Christiansen, H. Strunk
Grain orientation, texture, and internal stress optically evaluated by micro-Raman spectroscopy
Journal of Applied Physics, 101 (2007), p. 063531
- [25] M.D. Vaudin, Y.B. Gerbig, S.J. Stranick, R.F. Cook,
Comparison of nanoscale measurements of strain and stress using electron back scattered diffraction and confocal raman microscopy,
Applied Physics Letters 93 (19).
- [26] M. Vaudin, W. Osborn, L. Friedman, J. Gorham, V. Vartanian, R. Cook
Designing a standard for strain mapping: HR-EBSD analysis of SiGe thin film structures on si
Ultramicroscopy, 148 (2015), pp. 94–104
- [27] L.H. Friedman, M.D. Vaudin, S.J. Stranick, G. Stan, Y.B. Gerbig, W. Osborn, R.F. Cook
Assessing strain mapping by electron backscatter diffraction and confocal raman microscopy using wedge-indented si
Ultramicroscopy, 163 (2016), pp. 75–86
- [28] C.A. Kaufmann, R. Caballero, T. Unold, R. Hesse, R. Klenk, S. Schorr, M. Nichterwitz, H.-W. Schock
Depth profiling of Cu(In,Ga)Se₂ thin films grown at low temperatures
Sol. Energy Mater. Sol. Cells, 93 (6–7) (2009), pp. 859–863
- [29] W. Reimers, *Neutrons and Synchrotron Radiation in Engineering Materials Science*, Wiley-VCH Verlag GmbH & Co. KGaA, 2008, Ch. Introduction to Diffraction Methods for Internal Stress Analyses, pp. 113–135.
- [30] K.S. Knight
The crystal structures of CuInSe₂ and CuInTe₂
Mater. Res. Bull., 27 (2) (1992), pp. 161–167
- [31] C. Stephan, S. Schorr, H. Schock,
New Structural Investigations in the Cu₂Se(S)-In₂Se₃(S)/Cu₂Se(S)-Ga₂Se₃(S) Phase Diagrams, in:
Symposium M – Thin-Film Compound Semiconductor Photovoltaics–2009, Vol. 1165 of MRS Proceedings, 2009.

- [32] S.I. Wright, M.M. Nowell
Image Quality Mapping
Microsc. Microanal., 12 (2006), pp. 72–84
- [33] R. Keller, A. Roshko, R. Geiss, K. Bertness, T. Quinn,
EBSD measurement of strains in GaAs due to oxidation of buried AlGaAs layers,
Microelectronic Engineering 75 (1) (2004) 96–102, proceedings of the Symposium on
Characterization and Mechanical Reliability of Advanced Electronic Materials at Nanoscale, 2003
{ASME} Mechanics and Materials Conference.
- [34] V. Tong, J. Jiang, A.J. Wilkinson, T.B. Britton
The effect of pattern overlap on the accuracy of high resolution electron backscatter diffraction
measurements
Ultramicroscopy, 155 (2015), pp. 62–73
- [35] T. Britton, C. Maurice, R. Fortunier, J. Driver, A. Day, G. Meaden, D. Dingley, K. Mingard, A.
Wilkinson
Factors affecting the accuracy of high resolution electron backscatter diffraction when using
simulated patterns
Ultramicroscopy, 110 (12) (2010), pp. 1443–1453
- [36] H.-J. Bunge
2 - Orientation of Individual Crystallites
H.-J. Bunge (Ed.), Texture Analysis in Materials Science, Butterworth-Heinemann (1982), pp. 3–41
- [37] A. Winkelmann, C. Trager-Cowan, F. Sweeney, A.P. Day, P. Parbrook
Many-beam dynamical simulation of electron backscatter diffraction patterns
Ultramicroscopy, 107 (4–5) (2007), pp. 414–421
- [38] S. Theodoropoulou, D. Papadimitriou, K. Anestou, C. Cobet, N. Esser
Optical properties of $\text{CuIn}_{1-x}\text{Ga}_x\text{Se}_2$ quaternary alloys for solar-energy conversion
Semiconductor Science and Technology, 24 (1) (2009), p. 015014
- [39] J. González, M. Quintero, C. Rincón
Pressure dependence of the Raman A₁A₁ mode and pressure-induced phase transition in
 CuInSe_2
Phys. Rev. B, 45 (1992), pp. 7022–7025
- 40] L.I. Berger
Semiconductor Materials
CRC Press (1996)
- [41] A. Le Bail
Whole powder pattern decomposition methods and applications: a retrospection
Powder Diffraction, 20 (2005), pp. 316–326

- [42] J. Rodriguez-Carvajal
Recent advances in magnetic structure determination by neutron powder diffraction
Physica B: Condensed Matter, 192 (1–2) (1993), pp. 55–69
- [43] G.K. Wertheim, M.A. Butler, K.W. West, D.N.E. Buchanan
Determination of the gaussian and lorentzian content of experimental line shapes
Review of Scientific Instruments, 45 (11) (1974), pp. 1369–1371
- [44] J. Peyre, G. Principi
Linear combination of lorentzian and gaussian profiles to fit resonance spectra
Nuclear Instruments and Methods, 101 (3) (1972), pp. 605–606
- [45] D. Abou-Ras, S. Schorr, H.W. Schock
Grain-size distributions and grain boundaries of chalcopyrite-type thin films
Journal of Applied Crystallography, 40 (5) (2007), pp. 841–848
- [46] N.I. Medvedeva, E.V. Shalaeva, M.V. Kuznetsov, M.V. Yakushev
First-principles study of deformation behavior and structural defects in CuInSe₂ and Cu(In,Ga)Se₂
Phys. Rev. B, 73 (2006) 035207-1-6
- [47] M. Krejci, A.N. Tiwari, H. Zogg, P. Schwander, H. Heinrich, G. Kostorz
Rotational twins in heteroepitaxial CuInSe₂ layers on Si(111)
J. Appl. Phys., 81 (9) (1997), pp. 6100–6106
- [48] J. Aitchison, J.A.C. Brown
The lognormal Distribution
Cambridge University Press (1966)
- [49] T. Wada, T. Negami, M. Nishitani
Fivefold multiply twinned crystallites in CuInSe₂
Appl. Phys. Lett., 64 (3) (1994), pp. 333–335